The Astrophysical Journal, 629:204–218, 2005 August 10

ORBITS IN EXTENDED MASS DISTRIBUTIONS: GENERAL RESULTS AND THE SPIROGRAPHIC APPROXIMATION

Fred C. Adams[1,2] and Anthony M. Bloch[1,3]
Received 2005 January 19; accepted 2005 April 29

ABSTRACT

This paper explores orbits in extended mass distributions and develops an analytic approximation scheme based on epicycloids (spirograph patterns). We focus on the Hernquist potential $\psi = 1/(1 + \xi)$, which provides a good model for many astrophysical systems, including elliptical galaxies (with an $R^{1/4}$ law), dark matter halos (where N-body simulations indicate a nearly universal density profile), and young embedded star clusters (with gas density $\rho \sim \xi^{-1}$). For a given potential, one can readily calculate orbital solutions as a function of energy and angular momentum using numerical methods. In contrast, this paper presents a number of analytic results for the Hernquist potential and proves a series of general constraints showing that orbits have similar properties for any extended mass distribution (including, e.g., the NFW profile). We discuss circular orbits, radial orbits, zero-energy orbits, different definitions of eccentricity, analogs of Kepler's law, the definition of orbital elements, and the relation of these orbits to spirograph patterns (epicycloids). Over a large portion of parameter space, the orbits can be adequately described (with accuracy better than 10%) using the parametric equations of epicycloids, thereby providing an analytic description of the orbits. As an application of this formal development, we find a solution for the orbit of the Large Magellanic Cloud in the potential of our Galaxy.

Subject headings: galaxies: halos — galaxies: kinematics and dynamics — methods: analytical — stars: formation — stellar dynamics

1. INTRODUCTION

Orbits are a fundamental component of dynamical astrophysical systems, including dark matter halos, galaxies, star clusters, and solar systems. For a single point mass, the source term for a Keplerian potential, orbits are well-known conic sections and have been the cornerstone of solar system dynamics for centuries (starting with Newton 1687; for a modern treatment, see Murray & Dermott 1999). Many astrophysical systems have extended mass distributions, which give rise to more complex potentials and more complicated orbits (Binney & Tremaine 1987). Although an enormous amount of work has been done on understanding the dynamics of such extended mass distributions, the orbits themselves are not as well studied. In this paper we calculate the orbits for a class of extended mass distributions that provide good working models for dark matter halos, elliptical galaxies, and embedded young star clusters, albeit in rather different regimes of parameter space (see also van den Bosch et al. 1999 for a consideration of orbits in an isothermal potential). Along with our improved characterization of the orbits, we develop an effective analytic approximation scheme that describes the orbits in terms of epicycloids (spirograph patterns) and thereby obtain a set of parametric equations for the orbits. In addition to making dynamical calculations easier, this analytic approximation scheme adds to our conceptual understanding of the orbits—in much the same way that knowing Keplerian orbits are conic sections provides increased perception.

In this paper we focus on the Hernquist potential, which arises from a density profile of the form

$$\rho = \frac{\rho_0}{\xi(1+\xi)^3}, \qquad (1)$$

where the dimensionless radius $\xi = r/r_s$ and r_s is the length scale of the potential. This density profile has a corresponding analytic form for its distribution function (Hernquist 1990). One goal of this paper is to characterize the orbits for bodies traveling within this extended density distribution. The motivation for this effort is that particular subclasses of these orbits describe the motion of bodies in many astrophysical systems. The original application of this potential (Hernquist 1990) was to approximate the $R^{1/4}$ law for elliptical galaxies (de Vaucouleurs 1948). In addition, density profiles of this form appear in dark matter halos of galaxies and galaxy clusters, and in the molecular cloud cores that form stellar groups and clusters. Both of these latter applications require some explanation.

Over the past decade (starting with Navarro et al. 1997, hereafter NFW), numerical simulations of cosmic structure formation have shown that the density distributions of dark matter halos approach a nearly universal form (see also Crone et al. 1996; Moore et al. 1998; Bullock et al. 2001). Although the original form for this universal profile (NFW) is not as steep as that of equation (1) at large radii, subsequent work indicates that the Hernquist density profile provides a good description of the asymptotic structure of dark matter halos (Busha et al. 2003, 2004). One advantage of using equation (1) is that the total mass of the system is finite (whereas the integral of the original NFW density profile diverges). One long-term goal of structure formation studies is to understand the dynamics of these halo systems, including both the origin of the universal profile and its consequences. Toward that end, we must describe the orbital motions of test particles moving in the gravitational potential created by the universal density profile (where the "test particles" can range from individual dark matter particles with mass $m_W \sim 100$ GeV to small satellite galaxies with mass $M_{\rm sat} \sim 10^9\ M_\odot$).

Molecular cloud cores that form stellar clusters provide another application. They are inferred to have equations of state softer than isothermal (e.g., Larson 1985; Jijina et al. 1999) and hence density profiles of the approximate form $\rho \sim 1/r$, which

[1] Michigan Center for Theoretical Physics, Physics Department, University of Michigan, Ann Arbor, MI 48109.
[2] Astronomy Department, University of Michigan, Ann Arbor, MI 48109.
[3] Mathematics Department, University of Michigan, Ann Arbor, MI 48109.

coincides with the Hernquist density profile at small radii. The orbits found for the inner limit of the density profile (1) are thus applicable to star-forming regions. Most stars form in groups/clusters (Lada & Lada 2003; Porras et al. 2003), and subsequent stellar orbital motions determine the degree to which the environment affects star and planet formation (e.g., Adams & Myers 2001; Adams & Laughlin 2001).

Since the potentials considered here are spherically symmetric, motion is confined to a plane (in the absence of perturbations) and the orbits can be calculated to high accuracy using numerical methods. This paper takes a complementary approach and determines the nature of the orbits using analytic methods as far as possible and develops an analytic approximation scheme based on spirograph patterns. Our goal is to understand the orbits at the same level that we now understand Keplerian orbits, in spite of the greater mathematical complexity. Several subtleties arise that cannot be captured through numerical solutions alone. The orbital eccentricity can be defined in several ways, and each definition agrees with the Keplerian result in different aspects. The orbits do not close and their turning angles satisfy $\Delta\theta < \pi$ (for a half-orbit) and this angular deficit remains even in the circular limit. The maximum angular momentum, maximum turning angle, and radius of the circular orbit can all be determined analytically as a function of energy. These results allow for many properties of these orbits to be found analytically and add to our understanding of how the orbits depend on the underlying potential (see § 2).

Although a large number of results can be obtained analytically, a complete description of the orbital shapes requires numerical evaluation. Nonetheless, the orbit shapes are similar to the familiar form of epicycloids, often known as spirograph patterns (and not to be confused with epicycles; see below). This paper takes this analogy one step further (§ 3) and shows that for a large fraction of the relevant parameter space, the orbits in the Hernquist potential can be modeled with high accuracy (better than 10%) using the parametric equations of epicycloids. The resulting spirographic approximation provides an analytic description of the orbital shape. This analytic description, in turn, allows for other orbital quantities to be calculated analytically. For example, we show the effects of geometry on orbital decay by integrating $\Delta j/j$ over an orbit (§ 3.3), and we use the spirographic approximation to model the orbit of the Large Magellanic Cloud (LMC) in the potential of the Galaxy (§ 4).

In addition to the applications presented in this paper, the analytic approximations developed here can be used in a wide variety of other contexts. For example, an analytic description of the orbits can be useful in galactic stability theory (e.g., Evans & Read 1998), where the perturbed distribution function is given as an integral over the equilibrium orbit. Another application of analytic orbits is to find steady state distribution functions, which depend on the isolating integrals of motion (or the constants in the spirographic approximation developed here). This analytic description of orbits is also useful in assessing the effects of cluster environments on the star formation process. In this context, the orbits of newly formed stars determine how much radiation impinges on their circumstellar disks and their probability of experiencing scattering interactions; this physical process, in turn, determines how the cluster environment can compromise planet formation.

Although extended mass distributions do not always have the form of equation (1), we argue that the orbits found here provide good baseline models for orbital behavior in more general potentials. In particular, generic orbits in extended mass distributions will be more like those of the Hernquist model than the conic sections resulting from a Keplerian potential. Further, such generic orbits can be described through the spirographic approximation developed in this paper. Orbits in general extended mass distributions share a number of traits. For mass distributions of physical interest, the topology of the manifold of orbital solutions is simple (the same as the $S_1 \times S_1$ structure of the Kepler problem; see Smale 1970a, 1970b), although the geometry of the orbits is more complicated. One defining characteristic of these orbits—turning angles for a half-orbit bounded by $\pi/2 < \Delta\theta < \pi$—holds for general extended mass distributions (Contopoulos 1954). This paper proves additional results concerning generic orbits in extended mass distributions (§ 5). We show that the eccentricity can be defined in multiple ways, with the definitions coincident only for a Keplerian potential. We also show that orbital shapes in generalized extended mass distributions are confined to be relatively close to those of epicycloids (spirograph patterns). We validate this claim by finding a set of bounds on orbital shapes that apply to all physical potentials, and by explicit construction of orbits—and comparison with the spirographic approximation—for a collection of well-known potentials.

2. ORBIT SOLUTIONS

In this section we calculate orbits for bodies moving in the potential of the Hernquist profile (with the density distribution of eq. [1]). We define the total depth of the gravitational potential well $\Psi_0 \equiv 2\pi G\rho_0 r_s^2$ and the total mass $M_\infty \equiv 2\pi r_s^3 \rho_0$, so that the corresponding mass profile, force profile, and gravitational potential take the forms

$$M(\xi) = M_\infty \frac{\xi^2}{(1+\xi)^2}, \quad F(\xi) = \frac{\Psi_0/r_s}{(1+\xi)^2}, \quad \Psi(\xi) = \frac{\Psi_0}{1+\xi}. \tag{2}$$

All quantities are taken to be positive (with the proper signs inserted as necessary).

2.1. *General Orbits*

The basic formulation for orbits in spherical mass distributions is well known (Binney & Tremaine 1987); this section defines notation and presents analytic results for orbits in the Hernquist potential. An orbit in any potential $V(r)$ can be determined from the differential equation

$$\frac{d\theta}{dr} = \frac{1}{r}\left[\frac{2(E-V)r^2}{j^2} - 1\right]^{-1/2}, \tag{3}$$

where E is the energy and j is the specific angular momentum. This paper focuses on bound orbits with negative energy. We define dimensionless variables for the energy (ϵ) and angular momentum (q) according to

$$\epsilon \equiv |E|/\Psi_0, \quad q \equiv j^2/2\Psi_0 r_s^2. \tag{4}$$

The differential form of the orbit equation can then be written $\xi d\theta/d\xi = [q/f(\xi)]^{1/2}$, so that much of the dynamics is determined by the properties of the cubic equation

$$f(\xi) = -\epsilon\xi^2 + \frac{\xi^2}{1+\xi} - q. \tag{5}$$

For a given energy ϵ and angular momentum parameter q, the orbit exists within the range of ξ for which $f(\xi)$ is positive. The two positive zeros of $f(\xi)$ thus correspond to the radial turning points of the orbit and are denoted here as ξ_1 and ξ_2. The third

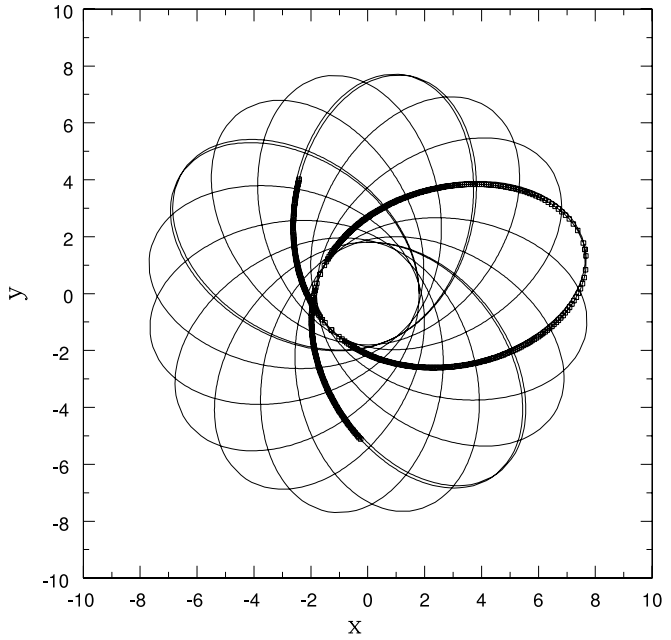

FIG. 1.—Example of an orbit in the Hernquist potential with energy $\epsilon = 0.10$ and angular momentum parameter $q = q_{\max}/2$. The orbit does not close and can be characterized by the angle through which the orbit turns during one radial oscillation. One part of the orbit is highlighted (*open squares*).

zero of the cubic is always negative for the physical range of parameter space, and we denote this root as $a \equiv -\xi_0 > 0$. Finding the roots of the equation (5) is straightforward but cumbersome (e.g., Beyer 1980). However, the inverse relations can be found simply:

$$\epsilon = \frac{\xi_1 + \xi_2 + \xi_1\xi_2}{(\xi_1 + \xi_2)(1 + \xi_1 + \xi_2 + \xi_1\xi_2)},$$
$$q = \frac{(\xi_1\xi_2)^2}{(\xi_1 + \xi_2)(1 + \xi_1 + \xi_2 + \xi_1\xi_2)},$$
$$a = -\xi_0 = \frac{\xi_1\xi_2}{\xi_1 + \xi_2 + \xi_1\xi_2}. \tag{6}$$

One quantity of interest for a given orbit is the angle $\Delta\theta$ through which the orbit turns over one half-cycle, e.g., as the orbit moves from ξ_1 to ξ_2. This angle is given by

$$\Delta\theta = \sqrt{q}\int_{\xi_1}^{\xi_2} \frac{d\xi}{\xi}\left[f(\xi)\right]^{-1/2}. \tag{7}$$

A related quantity of interest is the orbital half-period, denoted here as $\tau_{1/2}$. The natural timescale of this potential is $\tau_0 \equiv r_s(2\Psi_0)^{-1/2}$. The dimensionless timescale $\tilde{\tau}_{1/2} \equiv \tau_{1/2}/\tau_0$ can be written in integral form:

$$\tilde{\tau}_{1/2} = \int_{\xi_1}^{\xi_2} \xi\, d\xi\left[f(\xi)\right]^{-1/2}. \tag{8}$$

For a given dimensionless energy ϵ, orbits can have a maximum specific angular momentum and hence a maximum value of q. This maximum value takes the form

$$q_{\max} = \frac{1}{8\epsilon}\frac{(1 + \sqrt{1 + 8\epsilon} - 4\epsilon)^3}{(1 + \sqrt{1 + 8\epsilon})^2}. \tag{9}$$

In the limit of low energy $\epsilon \to 0$, we recover the Keplerian result $4\epsilon q_{\max} = 1$. In the opposite limit of $\epsilon \to 1$, we write $\epsilon = 1 - \delta$ and find the limiting form $q_{\max} = 4\delta^3/27$.

For a given energy ϵ, the minimum of the cubic function $f(\xi)$ is independent of the angular momentum variable q. The location of this minimum, denoted here by ξ_*, where $df/d\xi(\xi_*) = 0$, is given by

$$\xi_* = \frac{1 - 4\epsilon + \sqrt{1 + 8\epsilon}}{4\epsilon}. \tag{10}$$

In the limit of low energy $\epsilon \to 0$, we recover the Keplerian form $\xi_* = 1/2\epsilon$. As a result, we can identify ξ_* as playing the same role that the semimajor axis plays for bound orbits in Keplerian potentials (although these orbits are not ellipses). Note also that ξ_* is the radius of the circular orbit for a given energy ϵ.

For given values of energy and angular momentum (ϵ, q), the orbit takes a specified form. One such orbit is shown in Figure 1 for the case $\epsilon = 0.10$ and $q = q_{\max}/2$. For each half-oscillation in the radial direction, as ξ ranges from ξ_2 down to ξ_1, the orbit sweeps through an angle $\Delta\theta$, which lies in the range $\pi/2 \le \Delta\theta \le \pi$. In the Keplerian limit ($\epsilon \to 0$), $\Delta\theta \to \pi$. In the limit of radial orbits ($q \to 0$), the angle $\Delta\theta \to \pi/2$. Between these limits, the angular displacement takes on intermediate values that depend on energy and angular momentum. These results are illustrated in Figure 2, which shows $\Delta\theta$ as a function of $q/q_{\max}$ for a collection of energy values. One curious result is that the angle $\Delta\theta$ does not approach π in the limit of circular orbits (see eq. [16] below). For the set of curves shown in Figure 2, specifically for energy and angular momentum in the ranges $0.2 \le \epsilon \le 1$ and

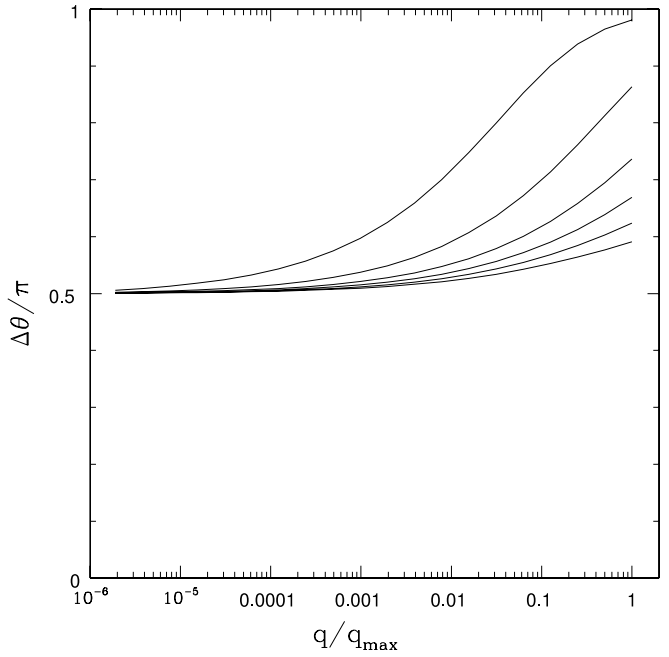

FIG. 2.—Turning angles for one-half of an orbit. The quantity $\Delta\theta$ is the angle through which the orbit turns as the radius varies from the inner turning point to the outer turning point. The turning angle $\Delta\theta$ for a half-orbit is plotted here as a function of $q/q_{\max}$, where $q_{\max}$ is the maximum angular momentum accessible for a bound orbit at a given energy. The various curves correspond to dimensionless energy values $\epsilon = 0.01$, 0.1, 0.3, 0.5, 0.7, and 0.9 (*from top to bottom*). Note that $\Delta\theta \to \pi/2$ in the limit $q \to 0$, but, in general, $\Delta\theta \ne \pi$ in the limit of circular orbits ($q \to q_{\max}$).

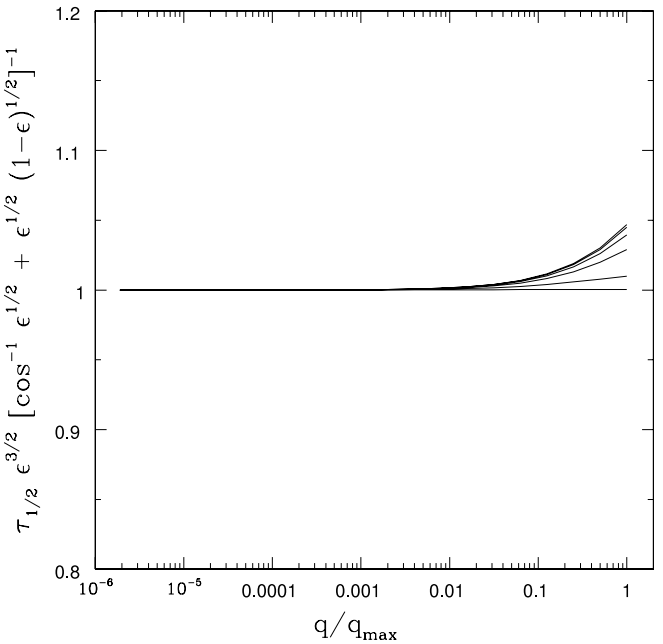

FIG. 3.—Range of orbital half-period. The quantity $\tilde{\tau}_{1/2}$ is the time required for the orbit to travel from the inner turning point to the outer turning point. Here the half-period is normalized by two functions: first, the factor $\epsilon^{3/2}$, which represents the variation expected in the Keplerian limit, and second, the factor $[\cos^{-1}\sqrt{\epsilon} - \sqrt{\epsilon}(1-\epsilon)^{1/2}]$, which gives the correct orbit time in the limit of zero angular momentum ($q \rightarrow 0$). The half-period is plotted as a function of q/q_{max}, where q_{max} is the maximum angular momentum accessible for a bound orbit at a given energy. The various curves correspond to dimensionless energy values $\epsilon = 0.01$, 0.1, 0.3, 0.5, 0.7, and 0.9 (*from bottom to top*).

$10^{-6} \leq q/q_{max} \leq 1$, the turning angle $\Delta\theta$ can be approximated with a fitting function of the form

$$\frac{\Delta\theta}{\pi} = \frac{1}{2} + \left[(1+8\epsilon)^{-1/4} - \frac{1}{2}\right]\left[1 + \frac{\ln(q/q_{max})}{6\ln 10}\right]^{3.6}. \quad (11)$$

This function provides an approximation to the turning angle with an accuracy of about 2.5% over the previously stated portion of parameter space.

Figure 3 shows the orbital half-period, i.e., the time required for the orbiting body to travel from the inner turning point to the outer turning point. In the figure, the half-period is normalized by the factor $\epsilon^{3/2}$, which represents the variation expected in the Keplerian limit, and by the factor $[\cos^{-1}\sqrt{\epsilon} - \sqrt{\epsilon}(1-\epsilon)^{1/2}]$, which gives the correct orbit time in the limit of zero angular momentum. The resulting (normalized) half-period is nearly independent of angular momentum and nearly the same as that of the radial orbit. The orbiting body spends most of its time at large ξ, where q has little effect, so the result is almost independent of q. The half-period does, however, depend on the energy ϵ.

Given an energy and angular momentum (ϵ, q), and hence the radial turning points, one can define a generalized "eccentricity" in terms of ξ_1 and ξ_2. Unlike the Keplerian case, the definition of eccentricity leads to some ambiguities. Two reasonable definitions of eccentricity are

$$e \equiv \frac{\xi_2 - \xi_1}{2\xi_*}, \quad \tilde{e} \equiv \frac{\xi_2 - \xi_1}{\xi_2 + \xi_1}. \quad (12)$$

At low energies $\epsilon \rightarrow 0$, the orbits become Keplerian and both definitions of the eccentricity coincide with the traditional one. In general, however, the two definitions do not coincide (see § 5.3). The first definition of eccentricity e has the advantage in that it includes the radius ξ_* of the circular orbit and the turning points represent symmetric departures from ξ_* (analogous to the Keplerian case). In contrast, the second definition $\tilde{e}$ does not correctly describe small departures about the circular orbit because $\xi_2 + \xi_1 \neq 2\xi_*$. On the other hand, the second definition allows for the full range of eccentricities $0 \leq \tilde{e} \leq 1$, whereas the first definition has a maximum eccentricity so that $0 \leq e \leq e_{max}$ (for all nonzero energies $\epsilon > 0$). This maximum eccentricity occurs for radial orbits ($q \rightarrow 0$), where the outer turning point $\xi_2 \rightarrow (1-\epsilon)/\epsilon$ and the inner turning point $\xi_1 \rightarrow 0$, and is given by

$$e_{max} = \frac{2(1-\epsilon)}{1 - 4\epsilon + \sqrt{1+8\epsilon}}. \quad (13)$$

In the Keplerian limit $\epsilon \rightarrow 0$, one recovers the expected result that $e_{max} \rightarrow 1$. In the inner limit $\epsilon \rightarrow 1$, one finds $e_{max} \rightarrow 3/4$. In between, the maximum eccentricity is a continuous monotonic function of dimensionless energy ϵ.

2.2. *Limiting Forms of the Solutions*

For the cases of circular orbits, radial orbits, and zero-energy orbits, the solutions reduce to limiting forms that can be readily evaluated. For circular orbits, one can solve for the relationship between the orbital period τ and radius. The resulting "Kepler law" for circular orbits takes the form

$$\tau^2 = \frac{2\pi}{G\rho_0}\xi(1+\xi)^2. \quad (14)$$

For a circular orbit at radius ξ, the energy and angular momentum are given by $\epsilon = (1+\xi/2)(1+\xi)^{-2}$ and $q = (1/2)\xi^3(1+\xi)^{-2}$. As a result, we can write the orbital period in terms of the dimensionless energy so that

$$\tau^2 = \frac{\pi}{G\rho_0}\frac{1}{\epsilon}\left(\frac{1+4\epsilon+\sqrt{1+8\epsilon}}{8\epsilon^2} - 1\right). \quad (15)$$

As defined here, the period τ is the time required for the orbit to make a complete circuit, i.e., for the angle θ to trace through 2π rad. However, the angular integral (eq. [7]) does *not* approach π in the limit of circular orbits (as it does for Keplerian orbits). The angular displacement is less than π and depends on energy according to

$$\lim_{q \rightarrow q_{max}} \Delta\theta = \pi(1+8\epsilon)^{-1/4}. \quad (16)$$

In the Keplerian limit $\epsilon \rightarrow 0$, $\Delta\theta \rightarrow \pi$, as expected. For $\epsilon \neq 0$, equation (16) agrees with the limit points of the curves shown in Figure 2. Since circular orbits are stable in this potential, small perturbations about the circular orbit lead to oscillations at the epicyclic frequency κ, which takes the form $\kappa^2 = 2\pi G\rho_0(3+\xi)\xi^{-1}(1+\xi)^{-3}$.

Another class of orbits that can be considered separately are those with zero angular momentum, i.e., radial orbits. In this case, the angular coordinate is no longer of interest and the orbits are characterized by their energy, ϵ. Each energy has a corresponding infall timescale τ, defined to be the time required to fall from the outer turning point ξ_2 to the center. This timescale can be evaluated to obtain the result

$$\tau = (4\pi G\rho_0)^{-1/2}\epsilon^{-3/2}\left(\cos^{-1}\sqrt{\epsilon} + \sqrt{\epsilon}\sqrt{1-\epsilon}\right). \quad (17)$$

For radial orbits, the position along the orbit is specified by the radial coordinate, so the angle θ is no longer necessary. Nonetheless, the angle of the orbit remains defined and the half-angle of the orbit (eq. [7]) reaches a definite limit. As $q \rightarrow 0$, we find $\Delta\theta \rightarrow \pi/2$.

Finally, we consider zero-energy orbits. For Keplerian potentials, such orbits are parabolas. Here the corresponding orbits are more complicated, but simple solutions can be found for limiting cases. The key parameter for a zero-energy orbit is its inner turning point, which is given by

$$\xi_1 = \frac{q + \sqrt{q^2 + 4q}}{2}. \tag{18}$$

One limiting form of this solution occurs when $\xi \ll 1$ for the entire orbit. This solution would also result for the case in which a density profile of the form $\rho \sim 1/r$ extends out to infinity. In this limit, the orbit equation can be solved to obtain $\sin\theta = \sqrt{q}/\xi$; i.e., the orbital path is a straight line defined by $y = \xi \sin\theta = \sqrt{q} =$ constant. For orbits that remain in the outer halo where $\xi \gg 1$, we can also simplify the expression to obtain

$$\cos\left[\left(\frac{q+1}{q}\right)^{1/2}\theta\right] = 1 - \frac{2(q+1)}{\xi}. \tag{19}$$

2.3. *Orbital Elements*

A particle in orbit can be described by six phase-space variables, which are usually taken to be the position vector $\boldsymbol{x} = (x,\ y,\ z)$ and the velocity vector $\boldsymbol{v} = (v_x,\ v_y,\ v_z)$. For the Kepler problem, one can replace these phase-space variables with osculating orbital elements, i.e., the elliptical (Keplerian) orbit that has the same instantaneous position and velocity vectors (Murray & Dermott 1999). For trajectories in extended mass distributions, the phase-space variables can be written in terms of the elements of the orbits found here. Since the potential is spherically symmetric and angular momentum is conserved, orbital motion is confined to a plane. The two angles that define the unit normal of the orbital plane (θ_p, ϕ_p) thus provide the first two orbital elements. The rest of this discussion is confined to this orbital plane. Although the assignment of the remaining orbital elements is not unique, we present a sensible prescription in what follows.

Within the plane, the orbital shape is determined by the energy ϵ and angular momentum, specified here by q. The pair (ϵ, q) thus can be used as the next two orbital elements. However, other choices are available. The energy ϵ can be replaced with the effective semimajor axis ξ_*, as defined by equation (10). For a given energy and angular momentum, the cubic equation (5) defines the turning points ξ_1 and ξ_2 of the orbit, so that the generalized eccentricity (eq. [12]) is well defined and can be used as the other variable. One can thus replace the variables (ϵ, q) with the pair (ξ_*, e), which provides the closest analogy to the Kepler problem. Alternately, one can use the turning points themselves, (ξ_1, ξ_2), to specify the orbital shape. Recall that the cubic equation that defines the turning points has three real roots in the regime of interest; because the problem has only two parameters (ϵ, q), specification of the turning points (ξ_1, ξ_2) is sufficient to define the equation, and the third root can be written in terms of the turning points (eq. [6]).

The two remaining orbital elements must specify the orientation of the orbit within the plane and the position of the particle along its orbit. In the custom of solar system dynamics, the term "longitude" is used to denote an angle that is measured relative to a fixed location in inertial space. Here we can specify the orientation of the orbit in terms of the longitude ϖ of the inner turning point ξ_1 (the longitude of pericenter). Like the elliptical orbits in the Kepler problem, the longitude of pericenter can precess. Unlike the case of the Kepler problem, orbits in extended mass distributions are not closed and the longitude ϖ of pericenter changes with every orbit. A full orbit turns through an angle $2\Delta\theta < 2\pi$, so the pericenter precesses backwards at the rate of $2(\pi - \Delta\theta)$ per orbit. The longitude of pericenter is given by $\varpi = 2(\pi - \Delta\theta)n + \varpi_0$, where ϖ_0 is the starting value ($t = 0$) and n is the number of full orbits that have elapsed. Note that we can use either the starting longitude ϖ_0 or the current longitude of pericenter ϖ as the next orbital element. For completeness, we can also define a continuous longitude of pericenter through the relation $\varpi_c \equiv 2(\pi - \Delta\theta)t/\tau + \varpi_0$, where τ is the (full) orbital period. Finally, the location of the particle along the orbit is given by its angular displacement θ. Again following the custom of solar system dynamics, the angular displacement variable can be called the "anomaly." The angle θ is thus the true anomaly and can be measured in two different ways. The natural definition is to measure θ from the inner turning point (or the outer turning point) for the current longitude of pericenter ϖ. However, one could also measure the angle with respect to the starting longitude of pericenter ϖ_0, in which case the anomaly is denoted as θ_0. We can also define a mean anomaly $M = \omega(\Delta t)$, where Δt is the time since pericenter passage and the mean motion variable $\omega \equiv (\Delta\theta)/\tau_{1/2}$ (see eqs. [7] and [8]).

TABLE 1
ORBITAL ELEMENTS

Shape Parameters	Orientation	Anomaly
(ϵ, q)	ϖ_0	θ_0
(ξ_*, e)	ϖ	θ
(ξ_1, ξ_2)	ϖ_c	M
(α, β, γ)	ϕ	$\hat{t}_p$

A collection of possible orbital elements is summarized in Table 1. Here we assume that the orbital plane is specified so that only four phase-space variables remain. The usual variables $[(x, y), (v_x, v_y)]$ can be replaced with various choices for the osculating orbital elements listed in Table 1. For each pair of shape parameters, any of the possible pairs for the orientation and anomaly are viable choices. The last line of the table lists the variables required to describe the orbit as an epicycloid (spirograph pattern), as discussed in the following section.

3. EQUIVALENT SPIROGRAPHIC ORBITS

The orbits found here for the Hernquist potential look much like epicycloids, more generally known as spirograph patterns. In this section we explore the relationship between the actual orbits and the closest equivalent spirographic orbits. We find a quantitative measure of the difference between the physical orbits and the spirographic approximation and show that the spirographic treatment is valid over a large portion of parameter space. This finding allows for a class of physical orbits to be described using simple parametric—and hence analytic—equations. The resulting analytic description facilitates a greater physical understanding of the orbital dynamics. For example, the effects of dissipation (friction) on the orbits can be modeled analytically using the spirographic approximation (see § 3.3).

The epicycloids discussed here are not the same as epicycles, which are often considered in connection with astronomical orbits. In the original Ptolemaic definition, an epicycle is the curve

generated by a small circle that rotates while it moves along the circumference of a larger circle. Epicycloids are curves generated by a smaller circle rotating inside (or outside) a larger circle, with a drawing point located a given distance away from the center of the smaller circle. In modern astronomy, the epicyclic frequency is the frequency of radial oscillation for a body in a circular orbit, when perturbed in the radial direction by an infinitesimal amplitude [so that $\kappa^2 = r^{-3} d(r^4\Omega^2)/dr$]. As a result, the inclusion of epicyclic motion (radial oscillations with frequency κ) provides a first-order correction to a circular orbit in an arbitrary potential [which determines the rotation curve $\Omega(r)$]. Many previous studies have explored the epicyclic approximation and the inclusion of higher order terms (e.g., Shu 1969; Kalnajs 1979; Dehnen 1999). In contrast, this present work explores epicycloids as approximations to physical orbits.

3.1. *Parametric Description of the Orbits*

In a fixed plane, here the orbital plane, the parametric equations for an epicycloid (a generalized spirograph pattern) can be written in the form

$$x(\hat{t}_p) = (\alpha - \beta)\cos\hat{t}_p + \gamma\cos\left[(\alpha - \beta)\hat{t}_p/\beta\right],$$
$$y(\hat{t}_p) = -(\alpha - \beta)\sin\hat{t}_p + \gamma\sin\left[(\alpha - \beta)\hat{t}_p/\beta\right], \quad (20)$$

where α is the radius of the larger spirograph circle, β is the radius of the smaller circle, and γ is the distance from the center of the smaller circle to the drawing point (e.g., see the World Wide Web site of D. P. Little,[4] which includes interactive drawing capability). These length scales should be considered dimensionless; they can be converted into physical units by specifying a length scale (r_s). Keep in mind that the variable $\hat{t}_p$ is a parameter and does not represent physical time (its relationship to time is elucidated below). With this form of the parametric equations, the spirograph pattern begins at $\hat{t}_p = 0$ with its maximum radius with an angle $\theta = \arctan(y/x) = 0$; the pattern then turns (counterclockwise) through an angle $(1 - \beta/\alpha)\pi$ as the radius decreases to its minimum value. The parametric variable $\hat{t}_p$ ranges from 0 to $\beta\pi/\alpha$ over this half-orbit. Note that the starting orientation of the orbit can be changed by including a starting phase angle ϕ (equivalent to an offset in the parametric time variable).

The parametric forms in equation (20) allow for two different (equivalent) representations of physical orbits (see below). In this treatment, we use the representation where γ plays the role of the semimajor axis. In this case, the transformation between the spirographic variables and the physical variables—and the inverse transformation—take the form

$$\xi_1 = \gamma - (\alpha - \beta), \quad \xi_2 = \gamma + (\alpha - \beta), \quad \Delta\theta = (\alpha - \beta)\pi/\alpha,$$
$$\gamma = \frac{1}{2}(\xi_1 + \xi_2), \quad \alpha = \frac{\pi}{2\Delta\theta}(\xi_2 - \xi_1), \quad \beta = \frac{1}{2}\left(\frac{\pi}{\Delta\theta} - 1\right)(\xi_2 - \xi_1). \quad (21)$$

Since the turning points ξ_1 and ξ_2 of the physical problem are related to the energy ϵ and angular momentum (specified by q) through equation (5), the above relations (eq. [21]) implicitly define the spirograph parameters in terms of the energy and angular momentum. The physical problem contains only two variables, which can be taken to be the energy and angular momentum (ϵ, q) or the turning points (ξ_1, ξ_2). The equivalent epicycloid is written in terms of three parameters (α, β, γ), but only two are independent. Any such triple will define an epicycloid, but only those related through equation (21) are physically relevant. The spirographic parameters are related to the energy and angular momentum of the orbit via

$$\epsilon = \frac{\gamma^2 + 2\gamma - (\alpha - \beta)^2}{2\gamma\left[(1 + \gamma)^2 - (\alpha - \beta)^2\right]}, \quad q = \frac{\left[\gamma^2 - (\alpha - \beta)^2\right]^2}{2\gamma\left[(1 + \gamma)^2 - (\alpha - \beta)^2\right]}. \quad (22)$$

Note that since $\xi_1,\ \xi_2 = \gamma \pm (\alpha - \beta)$, the parameter γ is akin to the semimajor axis of the orbit (although this analogy is not exact because the orbits are not ellipses). A natural definition of the eccentricity e_s for a spirographic orbit has the form

$$e_s = \frac{\alpha - \beta}{\gamma}. \quad (23)$$

Since $\gamma \geq (\alpha - \beta)$ for physically relevant orbits, the eccentricity $e_s \leq 1$.

In the Keplerian limit, the turning angle $\Delta\theta \to \pi$. Thus, the Kepler limit corresponds to the limit in which $\beta \ll \alpha$ and the turning points are given by $\xi_{1,2} = \gamma \pm \alpha$. In the limit of circular orbits, the above expressions (eqs. [22] and [23]) indicate that $(\alpha - \beta) \to 0$. However, in order for the parametric forms in equation (20) to trace a circle, the condition $(\alpha - \beta)/\beta \to 1$ $(\alpha/\beta \to 2)$ must also hold. In order for both of these limits to apply, $\alpha, \beta \to 0$. The limit of radial orbits is realized when the angular momentum vanishes, which requires $\gamma = (\alpha - \beta)$, and $\Delta\theta \to \pi/2$, which requires $\alpha = 2\beta$; as a result, radial orbits are given by $(\alpha, \beta,\ \gamma) = (2x,\ x,\ x)$ for any value of x.

The range of possible epicycloid patterns is much larger than the range of orbital shapes that represent physical motion (in the potential of an extended mass distribution). The allowed parameter space is depicted in Figure 4 (where the parameter γ is set equal to unity). For physical orbits, the turning angle for a half-orbit falls in the range $\pi/2 \leq \Delta\theta \leq \pi$; for our chosen representation, this constraint restricts the parameter space to the region $\beta < \alpha/2$. Since the inner turning point must be greater than zero, $\gamma > (\alpha - \beta)$. The allowed region of the α-β plane is thus bounded from above by the dashed line and from below by the dotted line. Above the dashed line where $\beta = \alpha/2$, the turning angle is too small and the resulting spirograph patterns are more open than those realized in physical potentials. Below the dotted line, the inner turning point is formally negative, so that the pattern turns "in front of" the center, rather than orbiting around it. The resulting pattern is tighter than those realized in physical orbits. The inset diagrams show the basic orbital shapes for the different regions of parameter space. Note that for this formulation, $\gamma > \alpha, \beta$, and the drawing point of these epicycloids extends beyond the smaller circle (so they cannot be drawn with conventional spirographic wheels).

The region of the α-β plane above the dashed line and below the dotted line (the upper right portion of Fig. 4) corresponds to the second representation of the orbits. In this region, the complementary epicycloid pattern has the same shape, turning points, and turning angle as the "original" pattern under the transformation

$$\gamma' = (\alpha - \beta), \quad (\alpha' - \beta') = \gamma,$$
$$\alpha'/\beta' = (1 - \beta/\alpha)^{-1}, \quad \hat{t}_p' = -(\alpha/\beta - 1)\hat{t}_p, \quad (24)$$

[4] D. P. Little (1997), available at http://www.math.dartmouth.edu/dlittle/java/SpiroGraph.

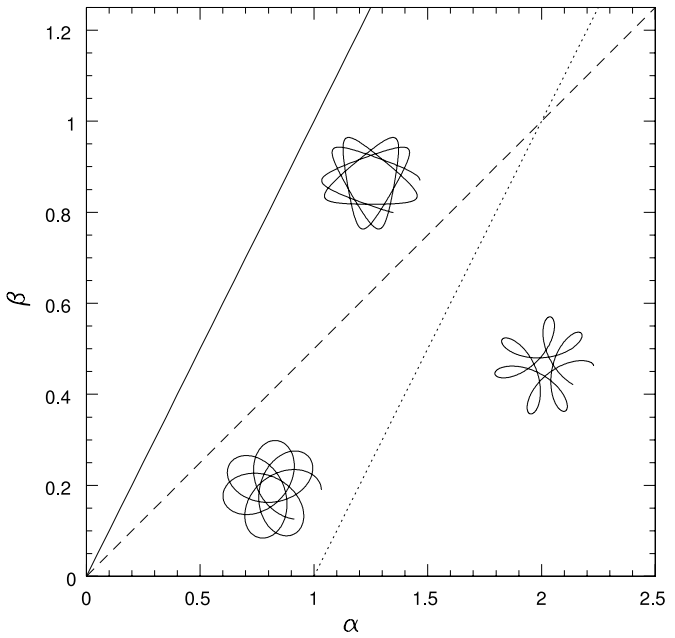

FIG. 4.—Allowed range of parameter space for spirographic orbits (epicycloids) to approximate physical orbits. The drawing point parameter γ, which plays the role of the semimajor axis, has been set equal to unity. The parameter α represents the radius of the larger circle, and β is the radius of the smaller circle. The value of β must lie below the dashed line (where $\beta = \alpha/2$) so that the turning angle of a half-orbit is greater than $\pi/2$. The β-value must also lie above the dotted line (where $\beta = \alpha - \gamma$) so that the inner turning point is positive. Physical orbits are confined to the region below the dashed line and above the dotted line. The inset diagrams show representative orbital shapes for the delimited regions of parameter space. The upper left portion of the diagram, above the solid line at which $\alpha = \beta$, is not allowed ($\beta < \alpha$ by definition). The upper right portion of the diagram (above the dashed line and below the dotted line) allows for an alternate representation of the physical orbits (see text).

where the primes denote the complementary variables. The sign transformation of the parametric time variable is necessary to make the spirographic pattern turn in the counterclockwise sense; the factor $(\alpha/\beta - 1)$ is not necessary, but it keeps parametric time passing at the same rate. For completeness, we note that epicycloids with $\beta < 0$ are also allowed and correspond to the smaller circle rotating on the outside of the larger circle (although such solutions are not considered here).

The parametric forms in equation (20) completely specify the geometry of the orbit (within the spirographic approximation). The velocity is given by the derivatives of the parametric equations with respect to physical time; i.e.,

$$v_x = -\left\{(\alpha - \beta)\sin\hat{t}_p + \gamma\left(\frac{\alpha}{\beta} - 1\right)\sin\left[\frac{(\alpha - \beta)\hat{t}_p}{\beta}\right]\right\}\frac{d\hat{t}_p}{dt},$$

$$v_y = \left\{-(\alpha - \beta)\cos\hat{t}_p + \gamma\left(\frac{\alpha}{\beta} - 1\right)\cos\left[\frac{(\alpha - \beta)\hat{t}_p}{\beta}\right]\right\}\frac{d\hat{t}_p}{dt}. \tag{25}$$

The direction of the velocity vector is thus determined (independent of the derivative $d\hat{t}_p/dt$) for any point along the orbit. Since the radial displacement is given by $\xi = (x^2 + y^2)^{1/2}$, the magnitude of the velocity is determined from conservation of energy, which can be written in the dimensionless form

$$v^2 = v_x^2 + v_y^2 = \frac{1}{1 + \xi} - \epsilon, \tag{26}$$

where $v^2(\text{physical}) = v^2(2\Psi_0)$. We can complete the description by using this result to find the variation of parametric time $\hat{t}_p$ with physical time t; i.e.,

$$\frac{d\hat{t}_p}{dt} = \left(\frac{1}{1 + \xi} - \epsilon\right)^{1/2} \times \left[\frac{\gamma^2(\alpha/\beta - 1)\alpha}{\beta} + \frac{(\alpha - \beta)^2\alpha}{\beta} - \left(\frac{\alpha}{\beta} - 1\right)\xi^2\right]^{-1/2}. \tag{27}$$

This expression gives $d\hat{t}_p/dt$ in dimensionless form. This formalism can be converted into physical units, where $d\hat{t}_p/dt$ has units of inverse time, using the fiducial timescale defined by $t_0^2 \equiv (r_s/2\Psi_0)$.

The full orbits in this problem sweep through the angular coordinate faster when the orbiting body is near the inner turning point (and slower near the outer turning point). In this approximation scheme, both the parametric expressions (eqs. [20] and [25]) and the conversion factor $d\hat{t}_p/dt$ have this qualitative behavior. In other words, some of the speed-up is accounted for in the parametric equations and the rest is contained in $d\hat{t}_p/dt$.

3.2. *Comparison with Physical Orbit Solutions*

One way to compare the dynamics of the physical problem and the spirographic approximation is to write the effective equations of motion in the same form. The equations of motion for the orbit problem itself are given in the text above. The equation of motion for the spirograph equivalent system can be written in the form

$$\frac{d\theta}{d\xi} = \frac{1}{\xi}\frac{\xi_1\xi_2 + (1 - 2\beta/\alpha)\xi^2}{\left[(\xi^2 - \xi_1^2)(\xi_2^2 - \xi^2)\right]^{1/2}}, \tag{28}$$

where $\xi = (x^2 + y^2)^{1/2}$ is the radial coordinate in the orbital plane. Here we consider the system to be spirograph equivalent if the orbits have the same turning points (ξ_1, ξ_2) and the same turning angle ($\Delta\theta$, which sets β/α).

Next we note that the equation of motion for both physical orbits and the spirographic orbits can be written in the form

$$\frac{d\theta}{d\xi} = \frac{1}{\xi}\left[(\xi - \xi_1)(\xi_2 - \xi)\right]^{-1/2} g(\xi), \tag{29}$$

where the functions $g(\xi)$ are slowly varying over the radial range of the orbits $\xi_1 \le \xi \le \xi_2$. We denote the functions $g(\xi)$ as "distortion functions" because they determine the manner in which the orbits are distorted from an elliptical shape. For physical orbits in a Hernquist potential and the corresponding spirographic approximation, the distortion functions $g(\xi)$ take the form

$$g_{\text{phys}}(\xi) = \left(\frac{q}{\epsilon}\frac{1 + \xi}{a + \xi}\right)^{1/2}, \quad g_{\text{spi}}(\xi) = \frac{\xi_1\xi_2 + (1 - 2\beta/\alpha)\xi^2}{\left[(\xi + \xi_1)(\xi + \xi_2)\right]^{1/2}}. \tag{30}$$

Note that for Keplerian orbits, one obtains the same general form as equation (29) with $g(\xi) = (q/\epsilon)^{1/2} = (\xi_1\xi_2)^{1/2} = \text{constant}$. The function g_{phys} reduces to this form in the limit $a \to 1$. The corresponding function g_{spi} approaches the Keplerian form in the limit of low energy ($\epsilon \to 0$) and high angular momentum ($q \to q_{\max}$).

Figures 5 and 6 show how closely the actual (physical) orbits can be approximated by the spirographic treatment developed

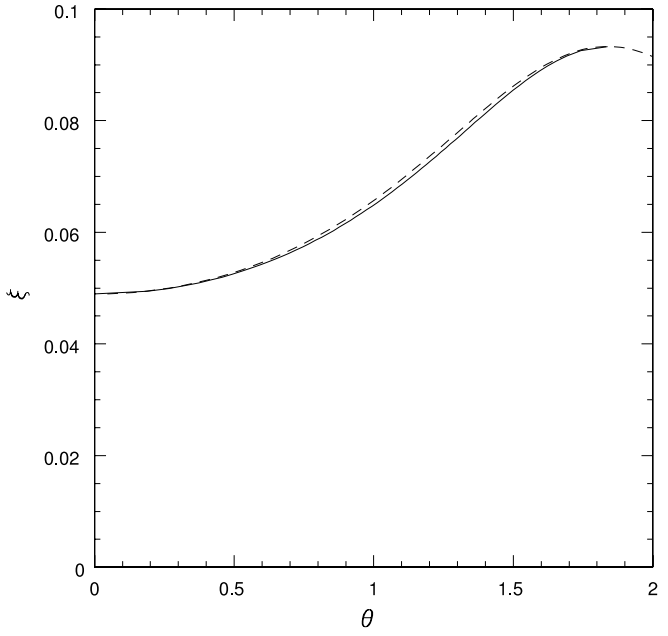

FIG. 5.—Comparison of the radial coordinate as a function of turning angle for the physical orbit problem in a Hernquist potential (*solid curve*) and the equivalent spirograph orbit (*dashed curve*). The two systems are chosen to have the same radial turning points (ξ_1 and ξ_2) and the same angular displacement per half-orbit $\Delta\theta \approx 1.84$ ($\Delta\theta/\pi \approx 0.585$). These values correspond to the energy $\epsilon = 0.90$ and the angular momentum variable $q/q_{\max} = 0.75$ for the Hernquist potential. According to the method of distortion functions developed in the text, the two orbit shapes differ by 2.2%; the spirographic orbit conserves angular momentum to an accuracy of 0.3%. For comparison, the shape of the physical orbit differs from that of a Keplerian orbit with the same turning points by 69%.

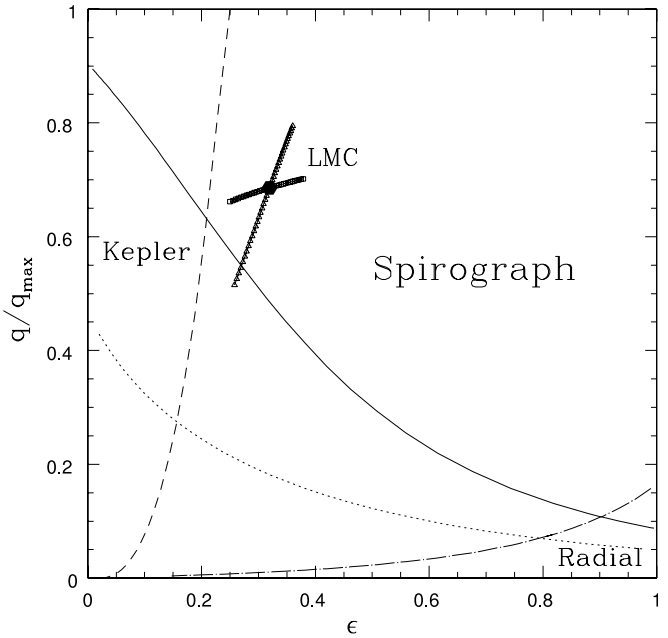

FIG. 6.—Regions of parameter space for which the Keplerian and spirographic approximations are valid for the Hernquist profile. The region of the ϵ-q plane above the solid curve corresponds to orbital parameters for which the rms deviation in the shape of the physical orbits from that of the spirographic approximation to the orbits is less than 10%. Similarly, the region above the dashed curve is where the rms deviation of the physical orbits from Keplerian orbits is less than 10%. The region above the dotted curve is where the spirographic approximation conserves the angular momentum of the orbit to an accuracy of 10%. Finally, the region below the dot-dashed curve is where the orbits are radial to within 10%. The large hexagon at $(\epsilon,\ q/q_{\max}) \approx (0.32,\ 0.69)$ marks our best estimate for the orbital parameters of the LMC. The accompanying (short) curves show the variation of the orbital parameters with variations in the Galactic scale radius r_s (*open squares*) and enclosed mass $M_{\rm in}$ (*open triangles*).

here. Figure 5 shows the radial excursion of an orbit, with the dimensionless radius plotted as a function of angle, for a physical orbit and the corresponding spirographic orbit. The two curves are nearly indistinguishable, which vindicates the approximation for this system ($\epsilon = 0.90$, $q/q_{\max} = 0.75$).

Next we need to quantify the difference between the physical orbits and the spirographic approximation to the orbits over the entire parameter space. We can characterize the available parameter space in terms of the quantities (ϵ, $q/q_{\max}$), where both variables have the range $0 \le \epsilon, q/q_{\max} \le 1$. The difference between the two orbits at a particular radius ξ can be measured by the quantity

$$\frac{\Delta g}{g} \equiv \frac{g_{\rm phys}(\xi) - g_{\rm spi}(\xi)}{g_{\rm phys}(\xi)}, \tag{31}$$

where the distortion functions g are defined above. The difference between two orbits can be measured by the rms of the difference $(\Delta g)/g$ averaged over an entire orbit, i.e., over the range of radii $\xi_1 \le \xi \le \xi_2$. For a benchmark comparison, we find the portion of parameter space for which the rms difference is less than 10%. This value of 10% is arbitrary. However, in many applications, such as the LMC orbit considered in the following section, the observational errors are typically in the range 10%–20%. The result is shown in Figure 6. For the region in the plane above the solid curve, the orbits can be represented as epicycloids (spirograph patterns) with an effective error less than 10%. Figure 6 also shows the portion of the ϵ-q plane for which the orbits are close to Keplerian in the same sense. The Kepler approximation is also characterized by a function g (see above), and the dashed curve marks the locus of points for which the Keplerian approximation differs from the physical orbit by 10%. The Keplerian approximation is thus valid only for the portion of parameter space to the left and above the dashed curve. The bottom portion of the ϵ-q plane shown in Figure 6 corresponds to low angular momentum and hence nearly radial orbits. The portion of parameter space below the dot-dashed curve can be modeled, again within 10%, as radial orbits (for which we have analytic solutions; see § 3.3). Note that for sufficiently deep orbits ($\epsilon \gtrsim 0.9$), the combination of the spirographic and radial approximations is sufficient to describe the orbits; this portion of parameter space corresponds to $\xi_* \lesssim 0.073$. Finally, the location of the orbit of the LMC is shown in the diagram and is found to be squarely within the spirographic regime (as discussed in § 4).

Another way to assess the validity of the spirographic approximation is to see how well the orbits conserve energy and angular momentum. Conservation of energy is built into the approximation (through the conversion factor $d\hat{t}_p/dt$) and is satisfied exactly. However, the spirographic orbits follow slightly different paths (than the physical orbits) and experience small variations in angular momentum over the course of an orbital cycle. Within the spirographic formalism, the angular momentum in dimensionless form is given by $j_{\rm spi} = |xv_y - yv_x| d\hat{t}_p/dt$, which can be written

$$j_{\rm spi} = \left(\frac{1}{1+\xi} - \epsilon\right)^{1/2} \times \frac{\gamma^2(\alpha/\beta - 1) - (\alpha-\beta)^2 + \gamma(\alpha-\beta)(\alpha/\beta - 2)\cos(\alpha\hat{t}_p/\beta)}{\left[\gamma^2(\alpha/\beta-1)^2 + (\alpha-\beta)^2 - 2\gamma(\alpha-\beta)(\alpha/\beta-1)\cos(\alpha\hat{t}_p/\beta)\right]^{1/2}}. \tag{32}$$

If the spirographic approximation were exact, this expression would be constant. In general, the approximation scheme leads to a small variation $(\Delta j)/j$ over the course of an orbit. The dotted curve in Figure 6 shows the trajectory in parameter space for which the angular momentum has an rms deviation of 10% over the course of an orbit. In the region above the curve—most of parameter space—the variation in angular momentum is less than 10%. Note that the requirement of angular momentum conservation, as enforced here, is less stringent than that of orbital shape, as measured by the distortion functions (compare the dotted and solid curves in Fig. 6). Since conservation of angular momentum is not precisely satisfied, the spirographic formalism does not provide an exact solution to any approximate physical problem; on the other hand, it does provide an extremely good approximation to the exact physical problem.

3.3. *Orbital Decay under a Frictional Force*

Within the spirographic approximation, we can calculate how orbits change under the action of a frictional force. As an example, we consider the frictional force $\boldsymbol{f}$ per unit mass to be proportional to the velocity so that

$$\boldsymbol{f} = -\frac{1}{T}\boldsymbol{v}, \tag{33}$$

where the leading coefficient is constant and T has units of time (this form applies to the low speed limit of dynamical friction; e.g., see Binney & Tremaine 1987). The torque exerted on the orbiting body is given by $\boldsymbol{r} \times \boldsymbol{f}$, and the time rate of change of the specific angular momentum j in terms of spirographic elements becomes

$$\frac{dj}{dt} = -\frac{r_s^2}{T}\left\{\eta\gamma^2 - (\alpha-\beta)^2 + (\alpha-\beta)\gamma(\eta-1)\cos\left[(1+\eta)\hat{t}_p\right]\right\}\frac{d\hat{t}_p}{dt}, \tag{34}$$

where $\eta \equiv (\alpha-\beta)/\beta$ and where the conversion factor $d\hat{t}_p/dt$ is given by equation (27), including the fiducial timescale t_0. The change in angular momentum over each half-orbit can be written

$$\Delta j = \int_0^{\tau_{1/2}} dt\,\frac{dj}{dt} = -\frac{r_s^2}{T}\int_0^{\beta\pi/\alpha} d\hat{t}_p\left\{\eta\gamma^2 - (\alpha-\beta)^2 + (\alpha-\beta)\gamma(\eta-1)\cos\left[(1+\eta)\hat{t}_p\right]\right\}, \tag{35}$$

where we have changed the variable of integration (to parametric time) in the second equality. This procedure allows us to evaluate the integral to obtain

$$\Delta j = -\frac{r_s^2}{T}\left[\eta\gamma^2 - (\alpha-\beta)^2\right]\left(\frac{\beta\pi}{\alpha}\right). \tag{36}$$

For comparison, in the limit of circular orbits (where $\alpha, \beta \to 0$, and $\eta \to 1$) the change in angular momentum reduces to $\Delta j = -(r_s^2/T)\gamma^2(\pi/2)$. This latter form is that expected from applying a constant torque over a specified time (a half-orbital period). The difference between the circular expression and equation (36) shows how the geometry of the orbit affects the decay of angular momentum. Within the spirographic approximation, this expression for the change in angular momentum is exact.

Next we consider the loss of orbital energy. The work done on the orbiting body by the frictional force over a half-orbit leads to a loss of energy, which can be written

$$\Delta E = \int \boldsymbol{f}\cdot\boldsymbol{v}\,dt = -\frac{r_s^2}{T}\int_0^{\tau_{1/2}} dt\left\{\gamma^2\eta^2 + (\alpha-\beta)^2 - 2\gamma\eta(\alpha-\beta)\cos\left[(1+\eta)\hat{t}_p\right]\right\}\left(\frac{d\hat{t}_p}{dt}\right)^2. \tag{37}$$

The integral can be simplified by changing the integration variable to parametric time. In this case, however, one factor of $d\hat{t}_p/dt$ is left over. Invoking the mean value theorem, we can pull the extra factor out of the integral and the expression for ΔE becomes

$$\Delta E = -\frac{r_s^2}{T}\left\langle\frac{d\hat{t}_p}{dt}\right\rangle\left[\gamma^2\eta^2 + (\alpha-\beta)^2\right]\left(\frac{\beta\pi}{\alpha}\right). \tag{38}$$

If we could identify the correct value of $\langle d\hat{t}_p/dt\rangle$, then the above expression would be exact within the spirographic formalism. In practice, we have to settle for an approximation; the mean value $\langle d\hat{t}_p/dt\rangle \approx (\beta\pi/\alpha\tau_{1/2})$ will suffice for most applications. In summary, the loss of energy per half-orbit becomes

$$\Delta E \approx -\frac{r_s^2}{T\tau_{1/2}}\left[\gamma^2\eta^2 + (\alpha-\beta)^2\right]\left(\frac{\beta\pi}{\alpha}\right)^2. \tag{39}$$

In addition to the approximation made in using the spirographic form (which typically leads to errors of a few percent), this expression for energy loss contains a few percent error incurred in the evaluation of the integral.

4. THE ORBIT OF THE LARGE MAGELLANIC CLOUD

As an application of the solutions found here, we consider the orbit of the LMC in the potential of the Galaxy. Using observational data in conjunction with the treatment developed above, we find the orbital elements of the LMC motion. The closest equivalent spirographic approximation reproduces the physical orbit to a precision of ~6%–7%, and we thereby obtain a parametric (and hence analytic) description of the orbit.

For this demonstration, we take the following observed quantities as given. The observed velocities of the motion of the LMC in Galactic coordinates (van der Marel 2002) are as follows: radial velocity $v_r = 84 \pm 7$ km s^{-1}, tangential velocity $v_\theta = 281 \pm 41$ km s^{-1}, and total velocity $v_T = 293 \pm 39$ km s^{-1}. The quoted errors lie in the range 8%–15% and result in uncertainties of comparable order in the derived quantities of the orbit. The distance to the LMC is now reasonably well known, with $r_{\rm lmc} \approx 50$ kpc (e.g., van der Marel 2002). We also need to specify the total mass $M_{\rm in}$ contained within the LMC orbit; using velocity data from a large number of Milky Way satellites, including the LMC, Kochanek (1996) finds $M_{\rm in} = (5 \pm 1) \times 10^{11}\,M_\odot$. These quantities are sufficient to specify the orbit within the framework developed here, i.e., assuming that the potential of the Galaxy can be modeled as a Hernquist potential over the range of radii probed by the LMC orbit. For completeness, we note that in order to reproduce the proper Galactic rotation curve at the solar circle, we would need to include additional disk/bulge components that

are neglected here (and which introduce another source of uncertainty in the orbital parameters).

Conservation of energy implies

$$\frac{1}{2}v_T^2 = \Psi_0\left(-\epsilon + \frac{1}{1+\xi_{\rm lmc}}\right) \approx \left(207 \text{ km s}^{-1}\right)^2, \quad (40)$$

where $\xi_{\rm lmc} = r_{\rm lmc}/r_s$. The scale Ψ_0 of the potential can be written in terms of known quantities:

$$\Psi_0 = \frac{GM_\infty}{r_s} = \frac{GM_{\rm in}}{r_{\rm lmc}}\frac{(1+\xi_{\rm lmc})^2}{\xi_{\rm lmc}} \approx \left(207 \text{ km s}^{-1}\right)^2\frac{(1+\xi_{\rm lmc})^2}{\xi_{\rm lmc}}. \quad (41)$$

We can solve the above two equations for the dimensionless energy ϵ to obtain

$$\epsilon = \frac{1+\xi_{\rm lmc}-\xi_{\rm lmc}/\mu}{(1+\xi_{\rm lmc})^2} \approx \frac{1}{(1+\xi_{\rm lmc})^2}, \quad (42)$$

where we have defined $\mu \equiv 2GM_{\rm in}/(r_{\rm lmc}v_T^2)$. The current observational estimates suggest that $\mu \approx 1$, which leads to the second approximate equality. Using the definition of q, we can write

$$q = \left[v_\theta^2\left(\frac{2GM_{\rm in}}{r_{\rm lmc}}\right)^{-1}\right]\frac{\xi_{\rm lmc}^3}{(1+\xi_{\rm lmc})^2} \approx \frac{0.92}{\mu}\frac{\xi_{\rm lmc}^3}{(1+\xi_{\rm lmc})^2}, \quad (43)$$

where we have used the observational results quoted above to obtain the numerical coefficient.

If the scale length r_s of the Galaxy and mass $M_{\rm in}$ are known, equations (42) and (43) specify the energy and angular momentum of the LMC orbit. The working estimate for $M_{\rm in}$ uses data from many satellites of the Milky Way (Kochanek 1996) and is reasonably secure (so that $\mu \approx 1 \pm 0.2$). We estimate r_s as follows. Numerical simulations of the formation of dark matter halos show that the density distributions approach a nearly universal form (NFW) when properly scaled. A recent numerical study (Navarro et al. 2004) indicates that the halo density profiles should be scaled so that they line up at r_{-2}, the radius at which the logarithmic slope of the density profile $s = d\log\rho/d\log r = -2$. The paper also shows that for halos with galactic masses (rotation velocities $\sim$200 km s^{-1}), the radius $r_{-2} = 18$–$28\ h^{-1}$ kpc. For the Hernquist density profile used here, the logarithmic slope $s = -2$ occurs at $\xi = \frac{1}{2}$, so that $r_s = 2r_{-2}$ (note that this relation is different for the original NFW profile, where $r_{-2} = r_s$). Using $h = 0.7$, we estimate the scale length of the Galaxy to be $r_s \approx 65$ kpc. As a result, $\xi_{\rm lmc} = r_{\rm lmc}/r_s \approx 0.77$ and our estimates for the energy and angular momentum of the LMC orbit are

$$\epsilon \approx 0.32, \quad q \approx 0.134\ (q/q_{\rm max} \approx 0.69). \quad (44)$$

The solid hexagon in Figure 6 marks the location of the LMC orbit in the plane of possible orbits. Note that the orbit falls within the region where the spirographic approximation is valid. The observed quantities used to estimate the orbital parameters are uncertain at the $\sim$10% level, so the resulting orbital elements are subject to comparable uncertainties.

Using the values of ϵ and q found here, we can specify the other parameters of the LMC orbit. The inner turning point $r_1 \approx 46$ kpc, the outer turning point $r_2 \approx 114$ kpc, and the effective semimajor axis of the orbit $r_* = r_s\xi_* \approx 82$ kpc. With these estimates for the turning points, the generalized eccentricities of the LMC orbit are $e = (\xi_2 - \xi_1)/(2\xi_*) \approx 0.41$ and $\tilde{e} = (\xi_2 - \xi_1)/(\xi_2 + \xi_1) \approx 0.43$.

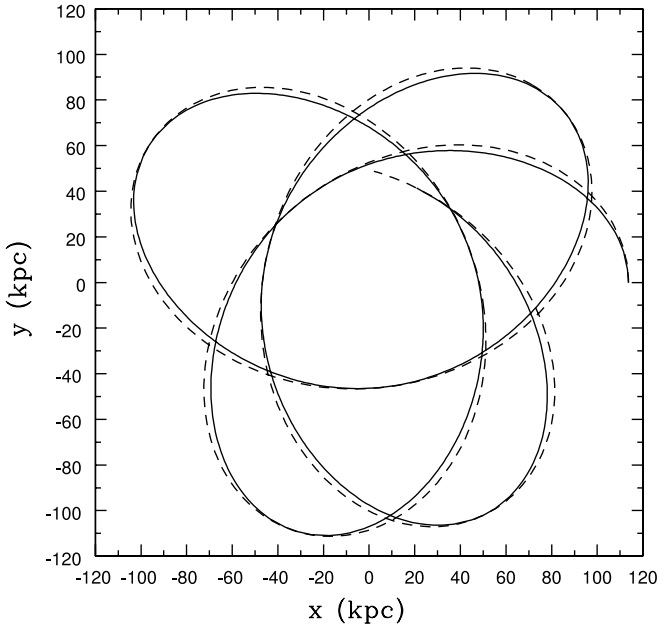

FIG. 7.—Predicted shape of the LMC orbit in the potential of the Galaxy. The coordinates x and y represent the plane of the orbit and are expressed in kiloparsecs. The solid curve shows the orbital shape for a Hernquist potential using our best estimate for the dimensionless orbital energy and angular momentum $(\epsilon,\ q/q_{\rm max}) = (0.32,\ 0.69)$. The dashed curves shows the spirographic (analytic) approximation to the orbit. The shape of the orbits agree to within about 7%, as measured by the distortion functions (eqs. [30] and [31]). As another measure, the analytic (spirographic) orbit conserves angular momentum to an accuracy of 1%. For comparison, the observational determination of the orbital parameters is subject to 10%–20% uncertainties.

The turning angle of the half-orbit is given by $\Delta\theta/\pi \approx 0.706$, so the orbit is far from closing. The total radial period $\tau \approx 1.75$ Gyr, which is comparable to the period of the equivalent circular orbit $\tau_c = 2\pi(r_{\rm lmc}^3/GM_{\rm in})^{1/2} \approx 1.5$ Gyr.

For the estimates of ϵ and q found here, the rms deviation of the physical orbit from its spirographic approximation is $\sim$6.6%. Because this difference is much smaller than the uncertainties in the orbit due to observational error and systematics, there is no practical difference between the actual physical orbit and its spirographic approximation. For comparison, the rms deviation of the physical orbit from the Keplerian approximation is much larger (about 17%). The spirographic orbital elements (in physical units) are thus $\alpha = 48$ kpc, $\beta = 14$ kpc, and $\gamma = 80$ kpc. The corresponding spirographic orbital eccentricity $e_s = (\alpha - \beta)/\gamma \approx 0.425$. Figure 7 shows an overlay of the physical orbit and its approximate form given by the spirographic formalism. The curves are shown in the orbital plane, and the phases of the orbits are aligned. The close agreement between the two orbits argues that the spirographic approximation is adequate for modeling the LMC orbit.

In the discussion thus far, we have assumed that the scale length r_s and mass $M_{\rm in}$ of the Galaxy within the radius of the LMC are known. The possible variation of these quantities provides an important source of uncertainty in the orbital elements. For example, if we assume that the scale length r_s is completely unknown, then equations (42) and (43) constrain the LMC parameters to lie along the curve defined by

$$q \approx 0.92(1-\sqrt{\epsilon})^3\epsilon^{-1/2}. \quad (45)$$

If we allow the scale length r_s to vary over the range $50 \le r_s \le 80$, bracketing the estimated value, the allowed orbits in the ϵ-q

plane lie on the locus of points marked by open squares in Figure 6. Similarly, we can vary the mass of the Galaxy within the current LMC position by varying the mass parameter μ in the above equations [$\mu \equiv M_{\rm in}/(5 \times 10^{11}\ M_\odot)$]. If we let the enclosed mass vary over its allowed range $\mu = 1 \pm 0.2$ (Kochanek 1996), the orbit lies along the locus of points marked by open triangles in Figure 6.

This analysis implies a lower limit on the mass $M_{\rm in}$. In order for the LMC to be in a bound orbit, $\epsilon > 0$ and equation (42) implies that

$$\mu > \frac{\xi_{\rm lmc}}{(1 + \xi_{\rm lmc})} = \frac{r_{\rm lmc}}{r_{\rm lmc} + r_s}. \tag{46}$$

The scale length r_s cannot be arbitrarily large. If we adopt a conservative upper limit on r_s based on the results of numerical studies (e.g., Navarro et al. 2004; Bullock et al. 2001), then $r_s < 100$ kpc and hence $\mu > \frac{1}{3}$. The corresponding mass limit becomes $M_{\rm in} > 1.7 \times 10^{11}\ M_\odot$. This limit is consistent with previous estimates of Kochanek (1996) and others (van der Marel 2002; Wilkinson & Evans 1999; Lin et al. 1995).

Next we apply the frictional formulas developed in § 3.3 to the orbit of the LMC (see also Murai & Fujimoto 1980). The above analysis determines the values for the spirographic parameters α, β, and γ. Using these results in equation (36), we find that the change in angular momentum over a half-orbit is given by $\Delta j \approx -3.12 r_s^2/T$. The angular momentum itself is given by $j = r_s(2q\Psi_0)^{1/2}$. Putting these results together with the parameters of the LMC orbit, we find that the fractional change in angular momentum per orbit is given by

$$\frac{\Delta j}{j} \approx -0.94 \left(\frac{T}{1\ {\rm Gyr}}\right)^{-1}. \tag{47}$$

The timescale T can be evaluated using previously known results (Binney & Tremaine 1987). The new result found here is that the change in angular momentum (per orbit) obtained using the true orbital shape, $\Delta j \propto [\eta\gamma^2 - (\alpha - \beta)^2]\beta/\alpha$, is larger than that of the equivalent circular orbit ($\Delta j \propto \gamma^2/2$) by 31%.

5. ORBITAL PROPERTIES FOR GENERAL MASS DISTRIBUTIONS

The discussion thus far has focused on orbits in the Hernquist potential and spirographic approximations to those orbits. In this section we show that a wider class of potentials leads to orbits with similar shape and can be adequately modeled using the spirographic approximation. Toward this end, we prove a series of results that apply to all physical potentials (§§ 5.1 and 5.3) and find the region of parameter space for which the spirographic approximation is valid for a collection of particular potentials (§ 5.2).

5.1. *General Constraints on Orbital Shape*

This section presents a set of general constraints on orbit shapes for any extended mass distribution. This set of constraints not only delimits the allowed orbital paths, but also shows that spirographic curves (epicycloids) provide reasonable approximations to the orbits for general extended mass distributions. The potential for any such mass distribution allows for two and only two turning points for bound orbits (Contopoulos 1954). This constraint limits the orbital path to lie within the annulus $\xi_1 \le \xi \le \xi_2$. We also know that the turning angle for a half-orbit is confined to the range $\pi/2 \le \Delta\theta \le \pi$ (Contopoulos 1954). To proceed further, we assume that the turning points and the turning angle (ξ_1, ξ_2, and $\Delta\theta$) are given, and find constraints on the path taken as the orbit travels from (ξ_2, 0) to (ξ_1, $\Delta\theta$) in the orbital plane. To illustrate these constraints, which are general, we plot one particular example in Figure 8. Here we use turning points $\xi_1 = 0.284$, $\xi_2 = 0.893$, and a turning angle $\Delta\theta = 2.01$ (for a Hernquist profile, these values correspond to the choices of dimensionless energy $\epsilon = 0.5$ and angular momentum $q/q_{\rm max} = 0.5$, but the constraints derived below hold for any physical potential).

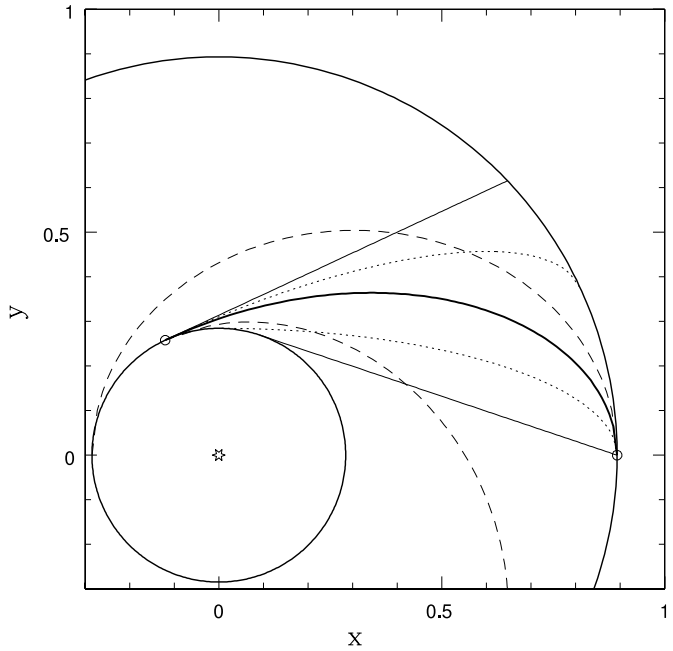

FIG. 8.—General constraints on orbital shape for an arbitrary potential. The boldfaced curve shows the spirographic orbit for given turning points (*open symbols, with radii marked by the inner and outer circles*) and a given turning angle for a half-orbit. The two solid lines represent an upper limit on how fast the orbit can turn, so that the orbit must trace a path between the two lines. Similarly, the dashed curves depict a limit on how slowly the orbit can turn; this limit corresponds to elliptical orbits and physical orbits must fall between these curves as well. The dotted curves represent the constraint that the orbit cannot turn any faster than the orbit of the uniform density model (which has $\Delta\theta = \pi/2$, and all orbits must have $\Delta\theta \ge \pi/2$). Physical orbits (for given ξ_1, ξ_2, $\Delta\theta$) must lie between the three pairs of constraints, thereby limiting the orbital shape to be reasonably close to that of the spirographic orbit.

One can show that the orbits contain no inflection points (S. Tremaine 2005, private communication). A related constraint can be found by using the definition of the turning angle and finding an upper bound on the magnitude of the derivative $|d\xi/d\theta|$. Since the potential is monotonic, $\psi \le \psi(\xi_1) = \epsilon + q/\xi_1^2$ over the radii of interest, and this bound takes the form

$$\left|\frac{d\xi}{d\theta}\right|_{\rm max} = \xi\left(\frac{\xi^2}{\xi_1^2} - 1\right)^{1/2}. \tag{48}$$

The integral of this quantity produces a curve of minimum radius ξ for a given angle θ, and this curve has the form

$$\xi(\theta) = \xi_1 \csc\left[\theta + \sin^{-1}(\xi_1/\xi_2)\right]. \tag{49}$$

This function starts at the outer turning point and reaches the inner turning point "as soon as possible," in the sense that any real orbit must travel inward more slowly as a function of angle θ. This argument produces a complementary limiting form—the orbit could stay at the outer turning point for as long as possible and then plunge inward (along a path of maximum $|d\xi/d\theta|$) just in

time to reach the inner turning point at $\theta = \Delta\theta$. The true orbit is confined to lie between the two aforementioned curves, which are shown as the solid lines in the illustrative example of Figure 8.

We can also consider the slowest possible turning of the orbit. The turning angle $\Delta\theta \leq \pi$ (Contopoulos 1954) and only attains the value of π in the Keplerian limit. The proof of this result shows that the magnitude of the derivative $|d\xi/d\theta|$ is always greater than that of the Keplerian orbit. As a result, the orbit must fall (from the outer turning point toward the inner turning point) faster than the Keplerian orbit with the same turning points, and the true orbit must lie within the Keplerian ellipse. As before, this argument provides a complementary constraint: if we construct a Keplerian orbit that has the same turning points and reaches the inner turning point at $\theta = \Delta\theta$, and trace the orbit backward out to the outer turning point, the physical orbit must lie outside the curve. The physical orbit must thus lie between these two ellipses, which are shown as dashed curves in Figure 8.

In general, as the density profile become less centrally concentrated, the turning angle decreases. In particular, $\Delta\theta = \pi$ in the limit of a point mass (the Keplerian limit), and the turning angle $\Delta\theta = \pi/2$ for a uniform density distribution ($\rho =$ constant). Since physical orbits are confined to have turning angle $\Delta\theta \geq \pi/2$, we argue that the uniform density orbit falls toward the inner turning point faster than any other case. The uniform density model thus provides a benchmark for comparison, and its orbits are determined by the function $f_c(\xi)$ defined by

$$f_c(\xi) = (\xi^2 - \xi_1^2)(\xi_2^2 - \xi^2). \tag{50}$$

We want to show that physical orbits are bounded by the orbit of the uniform density model, with the turning points ξ_1, ξ_2 chosen to coincide with those of the physical orbit. Consider the difference in angle between an arbitrary physical orbit [determined by $f(\xi)$] and the constant density benchmark case [determined by $f_c(\xi)$]. We define the difference in turning angle at a given radius to be $Q(\xi) \equiv \theta(\xi; f) - \theta(\xi; f_c)$, so that

$$Q(\xi) = \int_{\xi}^{\xi_2} \frac{d\xi}{\xi} \left(\frac{\sqrt{q}}{f^{1/2}} - \frac{\xi_1 \xi_2}{f_c^{1/2}} \right). \tag{51}$$

Now we look for the maximum angular difference. The derivative $dQ/d\xi = 0$ if and only if $f(\xi)/q = f_c(\xi)/(\xi_1\xi_2)^2$ at some intermediate point $\xi_1 < \xi < \xi_2$ [recall that $f/q = f_c/(\xi_1\xi_2)^2$ at the turning points ξ_1, ξ_2 by construction]. Next one can show that $f(\xi)/q = f_c(\xi)/(\xi_1\xi_2)^2$ at an intermediate point only if the second derivative of the physical potential $d^2\psi/d\xi^2$ is less than that of the constant density potential (since $d^2\psi_c/d\xi^2 < 0$ for the constant density case, "less than" means larger in magnitude and negative). Finally, we argue that the constant density potential has the greatest negative curvature of any physically relevant potential, so that the derivative $dQ/d\xi \neq 0$. This result implies that the difference in turning angle between any physical orbit and the orbit of the constant density potential must be monotonic. By inspection we find that Q is monotonically increasing. As a result, physical orbits are confined to lie outside the limiting curve found by integrating the orbit of a constant density potential (see eq. [50]); i.e.,

$$\theta(\xi) = \frac{\pi}{4} - \frac{1}{2} \sin^{-1} \left[\frac{(\xi_1^2 + \xi_2^2)\xi^2 - 2\xi_1^2\xi_2^2}{\xi^2(\xi_2^2 - \xi_1^2)} \right]. \tag{52}$$

As before, a complementary bound exists. Since the orbit cannot turn faster than equation (52), one can construct a solution in which the orbit stays at the outer turning point as long as possible and then follows a function of the form given in equation (52) to the inner turning point. Physical orbits must lie within such a curve. This argument leads to the pair of dotted curves shown in Figure 8.

The above constraints limit the trajectory taken by an orbit in any extended mass distribution. Each of the constraints leads to a pair of bounding curves, with the true physical orbit confined to lie between each pair of curves. The resulting combination of constraints implies an orbit much like that of the epicycloid (spirographic) curve. This set of constraints is illustrated in Figure 8 for one particular case, but this class of constraints holds for all orbits.

5.2. *Allowed Parameter Space for Specific Potentials*

Another way to illustrate the usefulness of the spirographic approximation is to explicitly calculate the allowed regions of parameter space for a collection of extended mass distributions. In addition to the Hernquist profile discussed above, we calculate orbits for three additional potentials and find the regimes of parameter space for which the spirographic approximation is valid. The first additional model is the NFW profile, where the density distribution and potential can be written in the dimensionless form

$$\rho = \frac{1}{\xi(1+\xi)^2}, \quad \psi = \frac{1}{\xi} \ln(1+\xi). \tag{53}$$

Next we consider a density distribution that is more concentrated and has the form

$$\rho = \frac{1}{\xi^{3/2}(1+\sqrt{\xi})^4}, \quad \psi = \frac{1}{(1+\sqrt{\xi})^2}. \tag{54}$$

We denote this case as the 3/2 model (from the power-law slope of its density profile in the inner limit). Like the Hernquist model, these potentials reach a finite central value, and we have scaled the dimensionless fields so that $\psi(0) = 1$. As a result, the energy ϵ is confined to the range $0 \leq \epsilon \leq 1$. For a given energy, each potential allows a maximum value $q_{\max}$ of the angular momentum parameter ($q_{\max}$ corresponds to a circular orbit) and the q parameter is confined to the range $0 \leq q/q_{\max} \leq 1$.

We also consider the Jaffe model, where the density profile has the form of a singular isothermal sphere for small radii, but falls more quickly at large radii and reaches finite total mass (Jaffe 1983). These profiles have the form

$$\rho = \frac{1}{\xi^2(1+\xi)^2}, \quad \psi = V_0 \ln\left(\frac{1+\xi}{\xi}\right). \tag{55}$$

Unlike the previous cases, this potential does not reach a finite value at the center, and hence the dimensionless energy ϵ does not have a finite range. The other potentials described above are defined over the energy range $0 \leq \epsilon \leq 1$ and allow orbits over the full radial extent $0 \leq \xi \leq \infty$. In order to compare the Jaffe model with these other potentials, we adopt the value $V_0 = \frac{1}{5}$; with this normalization, the orbits for $\epsilon = 1$ have an effective semimajor axis $\xi_* \approx 0.0041$ (instead of $\xi_* \to 0$).

For each potential defined above, we have calculated the orbits. For each physical orbit, we obtain the turning points (ξ_1, ξ_2) and turning angle $\Delta\theta$, and use the results of § 3 to define a spirographic approximation to the orbital path. The departure of the true orbit from its spirographic approximation is then calculated using the method of distortion functions developed in § 3.2. For these potentials, Figure 9 shows the region of parameter space

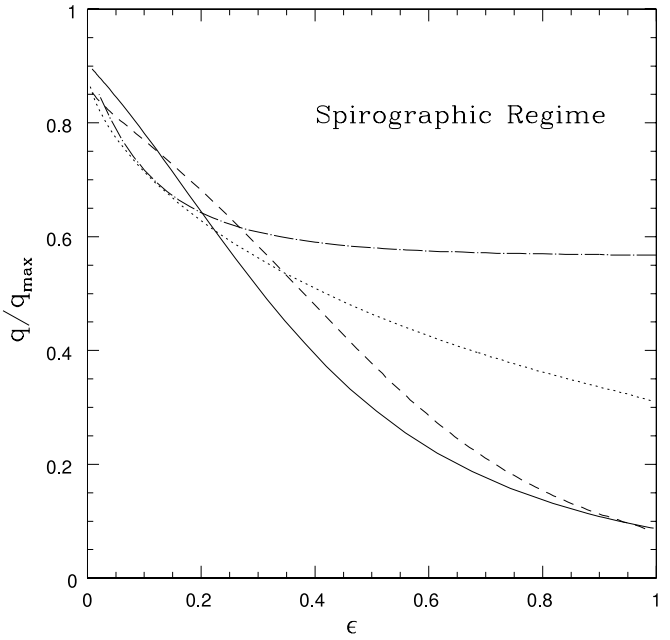

FIG. 9.—Regions of parameter space for which the spirographic approximation is valid for a collection of potentials. The region of the ϵ-q plane above the curves corresponds to orbital parameters for which the shape of the physical orbits deviates from that of the spirographic approximation by less than 10%. The potentials considered here are the Hernquist potential (*solid curve*), the NFW profile (*dashed curve*), the 3/2 model with density profile $\rho \sim \xi^{-3/2}(1+\sqrt{\xi})^{-4}$ (*dotted curve*), and the Jaffe model (*dot-dashed curve*). The Jaffe model differs from the other cases in that the potential does not reach a finite central value and hence the plane depicted here does not represent all of its parameter space.

for which the spirographic approximation to the orbits is valid, with an accuracy of (at least) 10%. The allowed region of the ϵ-q plane lies above the various curves: Hernquist profile (*solid curve*), NFW profile (*dashed curve*), the 3/2 profile (*dotted curve*), and the Jaffe model (*dot-dashed curve*; keep in mind that the parameter space for the Jaffe model extends beyond the portion of the ϵ-q plane shown here). At low energies corresponding to large radius orbits, the spirographic approximation has a limited range of validity for all of the potentials. At higher energy, the regime of parameter space for spirographic orbits depends on the degree of central concentration of the density profile. The Hernquist and NFW profiles have the same density dependence for small ξ ($\rho \sim \xi^{-1}$) and similar ranges of validity. In general, the region of validity of the spirographic approximation shrinks as the power-law index of the inner density profile increases (compare the previous models with the 3/2 model and the Jaffe model). This finding, that less centrally concentrated mass distributions give rise to orbits that are more spirographic in shape, can be understood from analytical considerations: in the limit of a uniform density distribution, the turning angle of the orbits has the value $\Delta\theta = \pi/2$ and the corresponding distortion function is identical to that of the spirographic approximation (see eq. [30] in the limit $\beta \to \alpha/2$). For completeness, we note that this analysis only considers the shape of the orbits. In order to provide a complete description of the dynamics, one must include the transformation between parametric time and physical time (the analog of eq. [27]), and this transformation depends on the potential.

Each potential also has a region of parameter space for which the Keplerian approximation is valid (these regions are not delimited here). The density profiles for the Hernquist and Jaffe models approach the form $\rho \sim \xi^{-4}$ at large radii and hence reach the Keplerian regime for sufficiently large ξ (low-energy ϵ). In contrast, the enclosed mass for the NFW profile diverges logarithmically and hence the Keplerian approximation is never applicable. The 3/2 model lies between these two cases, with a narrow regime of parameter space (at the low-ϵ edge of the plane) for which the Keplerian approximation is valid.

5.3. *Definitions of Orbital Eccentricity*

The definition of orbital eccentricity necessarily contains an ambiguity for extended mass distributions. Specifically, we show here that the two alternate definitions of eccentricity $e = (\xi_2 - \xi_1)/2\xi_*$ and $\tilde{e} = (\xi_2 - \xi_1)/(\xi_2 + \xi_1)$ are equivalent if and only if the potential is Keplerian. The first definition e measures eccentricity relative to the circular orbit given by ξ_* and has a maximum value $e_{\max} < 1$. The second definition $\tilde{e}$ is not centered on the circular orbit, but attains the full range $0 \le \tilde{e} \le 1$. The first half of the argument is well known—the two definitions of eccentricity are the same for a Keplerian potential.

To complete the argument, we suppose that the claim is true so that $e = \tilde{e}$. Then $\xi_1 + \xi_2 = 2\xi_*$, where ξ_* is the orbital radius of the circular orbit (for a given ϵ), and ξ_1 and ξ_2 are the turning points. For a general potential $\psi(\xi)$, the turning points are given by the zeros of the function $f(\xi)$, defined by

$$f(\xi) = -\epsilon\xi^2 + \xi^2\psi(\xi) - q. \tag{56}$$

The radius ξ_* of the circular orbit is given by the condition $df/d\xi = 0$. In order for $\xi_1 + \xi_2 = 2\xi_*$ to be valid for all orbits, the function $f(\xi)$ must be symmetric with respect to the point $\xi = \xi_*$; i.e., $f(\xi_* + x) = f(\xi_* - x)$ for all $x \in [0,\ \xi_*]$. If the function $f(\xi)$ is symmetric, all derivatives of odd order must vanish at $\xi = \xi_*$. The first derivative $df/d\xi$ vanishes by definition. The third derivative must also vanish and is given by

$$\frac{d^3 f}{d\xi^3} = \xi^2 \frac{d^3\psi}{d\xi^3} + 6\xi\frac{d^2\psi}{d\xi^2} + 6\frac{d\psi}{d\xi} = 0. \tag{57}$$

This condition does not depend on ϵ or q, but only on the form of the potential. Furthermore, the possible range of ϵ and q allow for all values of ξ_* to be realized. In order for the third derivative of $f(\xi)$ to vanish for all orbits, equation (57) must hold for all values of ξ. This differential equation is second order in the function $U \equiv d\psi/d\xi$ and has two linearly independent solutions: $U_{\rm A} = 1/\xi^2$ and $U_{\rm B} = 1/\xi^3$. The first solution corresponds to $\psi_{\rm A} \sim 1/\xi$, which is the Keplerian case. The second solution leads to $\psi_{\rm B} \sim 1/\xi^2$, which implies a negative mass density and is thus unphysical. The original differential equation (57) is third order and has a third solution, $\psi_C =$ constant, which is not of interest. Thus, we have shown that if $e = \tilde{e}$, then the potential $\psi = 1/\xi$ and is Keplerian. In order words, the validity of the condition $\xi_1 + \xi_2 = 2\xi_*$ requires a Keplerian potential.

6. CONCLUSION

This paper has explored orbital trajectories for the Hernquist potential and other extended mass distributions. Our results can be summarized as follows:

1. The first set of results quantitatively determines the orbits for the Hernquist potential. The analysis is straightforward. The orbits have a rosette shape (Fig. 1), as was well-known previously in qualitative terms (Binney & Tremaine 1987). The resulting orbits can be described by their turning angles $\Delta\theta$ and half-periods $\tau_{1/2}$ for a given value of energy ϵ and angular momentum q (see Figs. 2 and 3). In analogy to the Kepler problem, we have defined

osculating orbital elements (Table 1). The Hernquist profile allows for a number of results to be derived analytically. We have found the energy and angular momentum as function of the turning points (eq. [6]), the maximum angular momentum for a given energy (eq. [9]), a radial scale ξ_* that plays the role of the semimajor axis (eq. [10]), the analog of Kepler's law (§ 2.2), an analytic form for the turning angle in the limit of circular orbits (eq. [16]), and an expression for the radial period in the limit of low angular momentum (eq. [17]). This latter expression provides a good approximation to the radial period for all orbits (Fig. 3). We have also constructed a fitting formula (eq. [11]) that specifies the turning angle $\Delta\theta(\epsilon, q)$ as a function of energy and angular momentum over most of parameter space.

2. This paper shows that the physical orbits of the Hernquist profile can be modeled to a good approximation by epicycloid curves, more commonly known as spirograph patterns. These curves have analytic solutions, which can be written in the parametric form of equation (20). These parametric equations allow for a completely analytic description of the orbits, and we have developed this approximation in some detail. The transformation between spirographic orbital elements and physical parameters is given by equations (21)–(22). The effective eccentricity of a spirographic curve is given by equation (23). Most importantly, the spirographic approximation faithfully reproduces the shape of the physical orbits to an accuracy better than 10% over most of parameter space (Fig. 6). The spirographic approximation conserves energy exactly (using the transformation of eq. [27] to relate physical time to parametric time) and conserves angular momentum to a greater accuracy than it reproduces the orbital shape.

3. As a demonstration of the efficacy of this approach, we have found the shape of the orbit of the LMC as it traces through the halo of our Galaxy. If we model the Galactic potential with a Hernquist potential, the dimensionless energy and angular momentum of the LMC orbit are $(\epsilon,\ q/q_{\max}) = (0.32,\ 0.69)$ and the orbit takes the form shown in Figure 7. The spirographic approximation conserves angular momentum to an accuracy of 1% and reproduces the shape of the physical orbit to an accuracy of 6%–7%. These levels of error are much smaller than both the observational uncertainties in the problem and the errors incurred in approximating the Galaxy as a smooth, spherical, extended mass distribution. As a result, the analytic (spirographic) approximation provides a good working model for the orbit (with essentially no loss of accuracy).

4. In addition to considering orbits in the Hernquist potential, this paper argues that the results found here—in particular the spirographic approximation to the orbits—apply to general extended mass distributions. Toward this end, we have presented general constraints on the orbital shape (§ 5). Figure 8 shows that the orbits are restricted to be relatively close to the shape of an epicycloid for any extended mass distribution. Figure 9 shows that the spirographic approximation is valid over much of the ϵ-q plane for a collection of specific potentials (including the NFW profile). We have also shown that the definition of orbital eccentricity necessarily contains an ambiguity: for a given mass distribution, the eccentricity can either be defined to be symmetric with respect to a radial scale that plays the role of the semimajor axis or defined solely in terms of the turning points (see eq. [12]); the two definitions coincide only for a Keplerian potential (§ 5.3).

Many astrophysical systems involve orbits in extended mass distributions, and an analytic approximation to the orbits is often a useful tool. This paper develops the spirographic approximation, which can be used to model orbits in a wide variety of contexts. One such example, that of the LMC orbit, has been studied in this paper, but many additional applications of this formalism remain. Possible future topics include orbits of galaxies within their clusters, orbits of dark matter particles for dark matter detection strategies, globular cluster orbits in galactic potentials, orbits of small halos as they merge into larger halos during structure formation, orbits of young stars in their birth aggregates, and many others.

In addition to its direct applications, the approach developed here can be generalized in a number of ways. This work has focused on the Hernquist potential, although some comparison with other models has been included (see Fig. 9). Other cases should be considered and compared with the spirographic approximation. These include the HH model, in which two different Hernquist potentials are nested together (Ciotti 1996); models with varying degrees of central concentration (Tremaine et al. 1994); and models that include a point mass at the origin (to model the central black holes found in many galactic centers). For power-law potentials, the turning angles have already been computed (Touma & Tremaine 1997) and the spirographic approximation can be readily implemented. The orbits in this paper are confined to a single plane, for spherical potentials, but the spirographic approximation can be implemented for two-dimensional orbits in nonspherical potentials.

We note that the Hernquist potential and alternate forms (e.g., the NFW profile or the Jaffe model) are just models for more complicated physical structures. In the case of galactic halos, for example, the true potential must have corrections due to clumpiness and hence small-scale inhomogeneities, a galactic disk (or multiple disk components) and hence a large-scale quadrapole moment, perturbations from nearby large galaxies (e.g., Andromeda), and other complications. Many of these effects enter at the $\sim$10% level and imply 10% corrections to the orbital shape calculated from a spherical potential. This paper shows that over most of the relevant parameter space, the spirographic approximation leads to orbital shapes that agree with those of the Hernquist profile (and others; see Fig. 9) to an accuracy of better than 10%. Thus, in practice, the spirographic approach can be used as an approximation to the orbits without losing accuracy (compared to numerically calculated orbits) while providing an analytic description of the dynamics.

We would like to thank Dan Amidei, Michael Busha, Gus Evrard, Lars Hernquist, and Scott Tremaine for beneficial discussions and other useful input. We thank the referee for many useful comments that improved the manuscript. This work was supported at the University of Michigan by the Michigan Center for Theoretical Physics; by NASA through the *Terrestrial Planet Finder Mission* (NNG04G190G) and the Astrophysics Theory Program (NNG04GK56G0); and by NSF through grants DMS01038545 and DMS0305837.

REFERENCES

Adams, F. C., & Laughlin, G. 2001, Icarus, 150, 151
Adams, F. C., & Myers, P. C. 2001, ApJ, 553, 744
Beyer, W. H. 1980, Standard Mathematical Tables (Boca Raton: CRC Press)
Binney, J., & Tremaine, S. 1987, Galactic Dynamics (Princeton: Princeton Univ. Press)
Bullock, J. S., Kolatt, T. S., Sigad, Y., Somerville, R. S., Kravtsov, A. V., Klypin, A. A., Primack, J. R., & Dekel, A. 2001, MNRAS, 321, 559

Busha, M. T., Adams, F. C., Wechsler, R. H., & Evrard, A. E. 2003, ApJ, 596, 713
Busha, M. T., Evrard, A. E., Adams, F. C., & Wechsler, R. H. 2004, MNRAS, submitted
Ciotti, L. 1996, ApJ, 471, 68
Contopoulos, G. 1954, Z. Astrophys., 35, 67
Crone, M., Evrard, A. E., & Richstone, D. O. 1996, ApJ, 467, 489
Dehnen, W. 1999, AJ, 118, 1190
de Vaucouleurs, G. 1948, Ann. d'Astrophys., 11, 247
Evans, N. W., & Read, J. C. A. 1998, MNRAS, 300, 83
Hernquist, L. 1990, ApJ, 356, 359
Jaffe, W. 1983, MNRAS, 202, 995
Jijina, J., Myers, P. C., & Adams, F. C. 1999, ApJS, 125, 161
Kalnajs, A. J. 1979, AJ, 84, 1697
Kochanek, C. S. 1996, ApJ, 457, 228
Lada, C. J., & Lada, E. A. 2003, ARA&A, 41, 57
Larson, R. B. 1985, MNRAS, 214, 379
Lin, D. N. C., Jones, B. F., & Klemola, A. R. 1995, ApJ, 439, 652
Moore, B., Governato, F., Quinn, T., Stadel, J., & Lake, G. 1998, ApJ, 499, L5
Murai, T., & Fujimoto, M. 1980, PASJ, 32, 581
Murray, C. D., & Dermott, S. F. 1999, Solar System Dynamics (Cambridge: Cambridge Univ. Press)
Navarro, J. F., Frenk, C. S., & White S.D.M. 1997, ApJ, 490, 493 (NFW)
Navarro, J. F., et al. 2004, MNRAS, 349, 1039
Newton, I. 1687, Philosophia Naturalis Principia Mathematica (London: J. Streeter)
Porras, A., Christopher, M., Allen, L., Di Francesco, J., Megeath, S. T., & Myers, P. C. 2003, AJ, 126, 1916
Shu, F. H. 1969, ApJ, 158, 505
Smale, S. 1970a, Inventiones Mathematicae, 10, 305
———. 1970b, Inventiones Mathematicae, 11, 45
Touma, J., & Tremaine, S. 1997, MNRAS, 292, 905
Tremaine, S., et al. 1994, AJ, 107, 634
van den Bosch, F. C., Lewis, G. F., Lake, G., & Stadel, J. 1999, ApJ, 515, 50
van der Marel, R. P., Alves, D. R., Hardy, E., & Suntzeff, N. B. 2002, AJ, 124, 2370
Wilkinson, M. I., & Evans, N. W. 1999, MNRAS, 310, 645